

1 Ice Nucleating Particles Variability Across a Megacity

2
3 Sebastián Mendoza-Téllez¹, Karla Valdés², David Ramírez², Jan Alexis Cedillo³, Olivia
4 Rivera-Hernández⁴, Fernanda Córdoba¹, Harry Alvarez⁵, Javier Miranda⁶, Irma Rosas¹,
5 Graciela B. Raga¹, Emma Negrete¹, Leticia Martínez¹, Eva Salinas¹, and Luis A. Ladino^{1,*}

6
7 ¹Institute for Atmospheric Sciences and Climate Change, Universidad Nacional Autónoma de
8 México, Mexico City, Mexico

9 ²División de Ciencias Biológicas y de la Salud, Universidad Autónoma Metropolitana – Xochimilco,
10 Mexico City, Mexico

11 ³Escuela Nacional de Ciencias Biológicas, Instituto Politécnico Nacional, Mexico City, Mexico

12 ⁴Dirección de Monitoreo de Calidad del Aire, Secretaría del Medio Ambiente, Ciudad de
13 México, Mexico

14 ⁵Facultad de Ciencias, Universidad Nacional Autónoma de México, Mexico City, Mexico

15 ⁶Instituto de Física, Universidad Nacional Autónoma de México, Mexico City, Mexico

16
17
18 *Corresponding author: Luis A. Ladino (luis.ladino@atmosfera.unam.mx)

19 20 21 **Abstract**

22 Megacities are a major source of urban aerosol particles, which can impact cloud formation and
23 the local hydrological cycle. However, the aerosol-cloud interaction above megacities,
24 especially in their different microclimates, is poorly understood. In the present study, the
25 physicochemical and biological properties of urban aerosol particles, along with their ice
26 nucleating particle (INP) concentration via immersion freezing and as a function of particle size
27 (0.56 μm to 10 μm), were simultaneously characterized at two sites across the Mexico City
28 Metropolitan Area (MCMA). We found differences in the chemical composition, criteria
29 pollutants ($\text{PM}_{2.5}$, O_3 , CO , NO_x , and SO_2), and biological content between northern and
30 southern MCMA, separated by 16 km. The collected urban MCMA aerosol particles were found
31 to act as INPs, with average concentrations ranging between $0.04 \pm 0.04 \text{ L}^{-1}$ (at -15°C) and 24.9
32 $\pm 18 \text{ L}^{-1}$ (at -30°C). Although the measured INP concentrations were similar in both sites, the
33 southern samples showed a higher INP concentration for larger aerosol particles (i.e., particles
34 between 5.6-10 μm).

35 Although the urban aerosol's physicochemical properties, biological content, and its sources
36 were found to differ at both sites, it did not strongly impact the INP concentrations, with the
37 exception of the largest measured particles. This highlights the importance of considering that
38 aerosol-cloud interactions above a megacity may vary, especially when assessing the role of
39 INPs in cloud formation.

41 **1. Introduction**

42 Mexico City and its Metropolitan Area (MCMA) is one of the top megacities worldwide with
43 a population of 21 million inhabitants (Población, 2025). In the 1980s, the MCMA was reported
44 as the most polluted city on Earth (Molina and Molina, 2004); however, since the 1990s, air
45 quality has improved significantly (Lezama and Vargas, 2000). Even so, due to its size and the
46 diverse anthropogenic activities, the MCMA atmospheric processes are complex and far from
47 being completely understood (Molina et al., 2010). Nowadays, poor air quality is one of the
48 major threats for the MCMA inhabitants' health (Riojas-Rodríguez et al., 2014). The impact of
49 the high annual release of particulate matter (PM) (in the order of gigagrams, Gg) on the local
50 climate remains poorly quantified (Castro Romero et al., 2024).

51
52 Several studies have provided substantial insights into the physicochemical properties of PM
53 within the MCMA (Aldape et al., 1991; Edgerton et al., 1999; Doran et al., 2007; Querol et al.,
54 2008). For example, Vega et al. (2004) characterized the PM_{2.5} composition of the MCMA,
55 showing that the sulfate (SO₄²⁻), ammonium (NH₄⁺), and total carbon (elemental carbon +
56 organic carbon) average concentrations are higher in the north of the city compared to the
57 southern part (higher by 1.16 µg m⁻³ (18.1 %), 0.8 µg m⁻³ (23.6 %), and 18.49 µg m⁻³ (51.1 %),
58 respectively). This agrees with the data reported by the 2006 MILAGRO (Megacity Initiative:
59 Local And Global Research Observations) project, where a complete evaluation of the regional
60 and global impacts of Mexico's City atmospheric emissions was assessed (Molina et al., 2010).

61
62 Several studies found that organic matter has a huge impact on the MCMA's PM_{2.5}
63 composition. Amador-Muñoz et al. (2011) reported a carbon preference index (CPI) larger than
64 1 on the southwest of the MCMA, suggesting that this part of the city contains more biogenic
65 sources (Amador-Muñoz et al., 2013). Ladino et al. (2018) and Hernández-López et al. (2023)
66 reported clear differences in polycyclic aromatic hydrocarbons (PAHs) between the north and
67 south of the MCMA, with the highest concentrations reported in the northern part of the city.
68 Gasoline-fueled vehicles are likely responsible for local PAHs emissions and could reinforce
69 the presence of urban microclimates with independent local atmospheric processes, inside one
70 megacity (Molina and Molina, 2004).

71
72 A microclimate can be referred to as a relative small-scale area with a distinctive climate over
73 it as a whole (Met Office Factsheet 14). Owing to its large area, and the clear variability of land
74 use (e.g., industrial, rural, residential, commerce, and ecological preservation), the northern and

75 southern MCMA present significant differences in temperature (heat islands), rainfall, wind
76 patterns, humidity, aerosol and gas emissions, indicating the presence of a clear microclimate
77 differentiation (Met Office Factsheet 14; Molina and Molina, 2004; Amador-Muñoz et al.,
78 2013; Castro Romero et al., 2024). Although the studies above highlight the clear differences
79 in the sources and physicochemical properties of PM in different parts of the MCMA, studies
80 that include simultaneous measurements at two or more sites are scarce. This is of high
81 importance to understand the microclimates along the MCMA and their relationship with local
82 precipitation events. Zhu et al. (2024) evaluated precipitation events across China, finding that
83 precipitation characteristics could differ across climatic zones. Additionally, Li et al. (2019)
84 showed that atmospheric circulation changes driven by global warming modulated the
85 intensification of extreme precipitation events across North America.

86
87 Meteorological data and models indicate a predominance of northerly, southerly, southwesterly,
88 and northeasterly wind events in MCMA, with frequencies of 20 %, 16 %, 15 %, and 13 %,
89 respectively (Celada-Murillo et al., 2013). In addition, typically wind events with speeds
90 ranging from 0.25 to 1.50 m s⁻¹ appear mainly during the early morning, while other wind events
91 with larger speeds (i.e., ranging from 1.5 to 5.50 m s) appear mainly during the afternoon and
92 night (Celada-Murillo et al., 2013; Salcido et al., 2015). On the other hand, meteorological
93 conditions in some defined area, as the presence of atmospheric stable conditions, or the well-
94 known large-scale atmospheric circulation could help understanding the real perturbations of
95 urban aerosols on cloud formation and precipitation events (Trofimov et al., 2022).

96
97 Given that most of the precipitation over the tropics comes from ice-containing clouds
98 (Mülmenstädt et al., 2015) and that aerosol particles acting as ice nucleating particles (INPs)
99 are key in mixed-phase cloud (MPC) formation (Rogers and Yau, 1996; Houze, 2014; Kanji et
100 al., 2017), information on the interplay between aerosol particles and cloud formation in big
101 cities such as the MCMA is urgently needed, especially because extreme precipitation events
102 are predicted to increase with time (Tabari, 2020; Gimeno et al., 2022), causing huge
103 economical and societal impacts in densely populated cities. Aerosol particles have the potential
104 to influence the development of deep convective clouds, which are typically associated with
105 extreme rainfall events (Burrows et al., 2022). Efficient INPs can promote specific processes
106 as the seeder-feeder mechanism (Ohneiser et al., 2025) triggering primary ice particle formation
107 as well as ice multiplication, increasing the ice water content in MPC (Purdy et al., 2005). These
108 ice particles can grow at expenses of the surrounding water droplets, via the Wegner-Bergeron-

109 Findeisen process, enhancing precipitation rates (Heymsfield et al., 2020; Ohneiser et al.,
110 2025). Toll et al. (2024) showed that the presence of anthropogenic particles hot spots can
111 modify cloud microphysics, leading to cloud glaciation and precipitation events under
112 stratiform non-convective clouds.

113

114 The impact of urban particles on ice formation in MPCs is well documented (e.g., Hasenkopf
115 et al., 2016; Pereira et al., 2021; Chen et al., 2024). For example, Zhao et al. (2019) reported
116 that the presence of urban aerosol particles affects the microphysical properties of clouds under
117 moderate convective conditions, decreasing ice crystal number concentration (ICNC) and thus
118 increasing the ice particle effective radius (R_{ei}). Chen et al. (2024) found that urban super-
119 micron traffic-influenced road dust and construction-related dust particles were the primary
120 source of INPs (heat-resistant INPs) at temperatures below $-15\text{ }^{\circ}\text{C}$ in Beijing, China.
121 Nevertheless, given that urban aerosol particles are a complex multicomponent mixture (i.e.,
122 biological, dust, black carbon, and biomass burning (BB) particles, among others), they may
123 contain components with contrasting ice nucleation abilities. Although urban centers clearly
124 experience high aerosol concentrations, INP concentrations in megacities do not necessarily
125 increase during heavily polluted periods (e.g., Bi et al., 2019; Cabrera-Segoviano et al., 2022;
126 Chen et al., 2024).

127

128 The role of urban particles emitted in the MCMA in ice-cloud formation has been previously
129 evaluated (Knopf et al., 2010; Pereira et al., 2021; Rodríguez-Gómez, 2021; Cabrera-Segoviano
130 et al., 2022; Melchum et al., 2023). The first ice nucleation study in the MCMA was conducted
131 by Knopf et al. (2010) as part of the MILAGRO project. The authors reported that the particles
132 in the northern part of the City are dominated by organics, and can efficiently act as INP under
133 cirrus and MPC conditions, i.e., relative humidity with respect to ice (RH_{ice}) of $\sim 105\%$ to 150%
134 and temperatures of 205 K to 255 K .

135

136 Regarding MPC, Pereira et al. (2021) found that the ubiquitous anthropogenic emissions did
137 not have a significant impact on the INP concentrations, with samples collected in rural and
138 urban sites, both in the south of the MCMA. Cabrera-Segoviano et al. (2022) reported an inter-
139 annual variability of INP concentrations (a one order of magnitude difference at temperatures
140 higher than $-20\text{ }^{\circ}\text{C}$) at southern MCMA between 2018 and 2019, a fact that can be related to the
141 variability in aerosol emissions like re-suspended dust. Rodríguez-Gómez (2021) reported
142 higher INP concentrations in the planetary boundary layer compared to the free troposphere on

143 samples collected in southern MCMA during the BB season, similar to previous studies (Prenni
144 et al., 2012; Jahn et al., 2020; Jahl et al., 2021). Finally, Melchum et al. (2023) evaluated the
145 INP abilities of different airborne microorganisms from tropical places such as MCMA and other
146 sites across Mexico. The authors found that out of the 64 tested microorganisms, only the
147 *Cupriavidus pauculus* (proteobacteria) and the *Phaeocystis* sp. (marine phytoplankton) can be
148 relevant to MPC formation (with onset freezing temperatures of -11.8 °C and -16.0 °C,
149 respectively).

150

151 Although PM and INPs have been previously characterized in the MCMA, simultaneous INP
152 measurements at more than one site have never been reported. Therefore, there is a poor
153 understanding of how urban aerosol particles could influence cloud formation across the
154 different MCMA's microclimates. To fill this gap in knowledge, the present study reports the
155 simultaneous characterization (physical, chemical, and biological) of PM_{2.5} as well as the INP
156 concentration in a northern and a southern site within the MCMA. To the best of our knowledge,
157 this is the first time that such comprehensive evaluation of the aerosol-cloud interactions is
158 performed in this megacity.

159

160 **2. Methods**

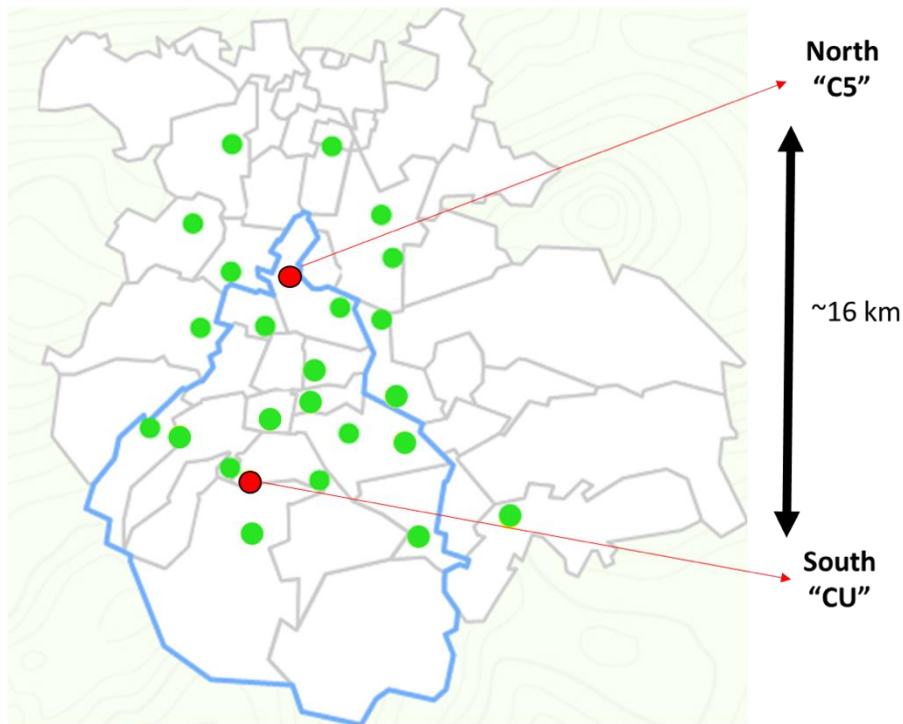
161 **2.1 Sampling location**

162 Mexico City is a tropical city located at 2240 m a.s.l. (Población, 2025), with a particular
163 topography that influences the accumulation of air pollutants (Molina and Molina, 2004). With
164 a sub-humid climate, the city presents an average annual temperature (between 1950 and 2013)
165 of 15 to 18 °C (Behzadi et al., 2020). The MCMA experiences three different seasons such as
166 cold-dry: October-February, warm-dry: March-May, and wet season: June-October. The mean
167 annual precipitation within 1950–2013 for Mexico City was reported to vary between 357 mm
168 year⁻¹ and 1298 mm year⁻¹ (Jáuregui, 2000; Molina et al., 2009; Behzadi et al., 2020; Cabrera-
169 Segoviano et al., 2022).

170

171 A short-term field campaign was carried out simultaneously at the north and south of the
172 MCMA during the dry-warm season, i.e., between May 12th and May 20th, 2022. Both
173 sampling sites are located within Mexico City (Fig. 1), and they are ~16 km away from each
174 other.

175



176

177 Figure 1. Location of the MCMA showing Mexico City (blue contour) as well as northern and
 178 southern sampling sites (red circles). The green circles represent the Mexico City atmospheric
 179 monitoring stations. Modified from <https://aire.cdmx.gob.mx/>

180

181 Sampling at the southern site (CU, 19.3262° N 99.1761° W) took place on the roof of the
 182 Institute for Atmospheric Sciences and Climate Change building (approx. 15 m a.g.l.), on the
 183 main campus of the Universidad Nacional Autónoma de México (UNAM). Traffic is the
 184 primary source of anthropogenic pollution at this site. However, an ecological reserve (237 ha)
 185 is located within the main UNAM campus, with the vegetation being dry and brown and
 186 susceptible to forest fires during the sampling period. It can provide biological material to the
 187 atmosphere through the native and introduced species of plants, animals, and microorganisms
 188 that live in it (Melchum et al., 2023).

189

190 On the other hand, the sampling at the northern site (C5, 19.483781° N 99.147312° W) took
 191 place on the roof of the Environmental Analysis Laboratory (C5) building (approx. 5 m a.g.l.)
 192 of the Mexico City Atmospheric Monitoring System (<http://www.aire.cdmx.gob.mx/>). The C5
 193 sampling site is subject to a wide range of anthropogenic sources, as it is located in the city's
 194 popularly known “industrial area.” Traffic, industrial, and other anthropogenic emissions
 195 contribute to high PM atmospheric concentrations at this sampling site (Castro Romero et al.,
 196 2024).

197

198 Meteorological (T, RH, wind direction, wind speed, solar radiation, and precipitation) and
 199 criteria pollutants (PM_{2.5}, O₃, CO, NO_x, and SO₂) data were recorded on both sites during the
 200 sampling campaign (Tables S1 and S2, and Figs. S1 and S2). The campaign dates, total
 201 sampling times and volumes are shown in Table 1. The ionic composition and elemental
 202 composition were obtained using ion chromatography and X-ray fluorescence, respectively, on
 203 the 24-hour collected samples. Culturable microorganisms were obtained through different
 204 microbiological analysis described in section 2.2.5, on 5 min collected samples.

205

206 Table 1. Sampling campaign description: dates, total sampling times, and sampling volume are
 207 shown for the three sampling methods: MiniVol (2.5 µm cut-off) for chemical analysis,
 208 MOUDI (0.56 to 10 µm cut-off, see section 2.2.6) for INP analysis, and BioStage (10 µm cut-
 209 off) for biological analysis. Note that the sampling times were the same at both sites.

SAMPLING CAMPAIGN								
Date (month- day- year)	MiniVol ¹ (chemical analysis)		MOUDI ² (INP analysis)				BioStage ³ (biological analysis)	
	Total sampling time (h)	Sampling volume (m ³)	Initial sampling time (local time, h)	Final sampling time (local time, h)	Total sampling time (h)	Sampling volume (m ³)	Total sampling time (h)	Sampling volume (m ³)
05-12-22	24	7.2	-	-	-	-	0.08	0.1
05-13-22	24	7.2	-	-	-	-	0.08	0.1
05-14-22	24	7.2	-	-	-	-	0.08	0.1
05-15-22	24	7.2	-	-	-	-	0.08	0.1
05-16-22	24	7.2	8:37	12:58	4:21	7.8	0.08	0.1
05-17-22	24	7.2	8:20	12:20	4:00	7.2	0.08	0.1
05-18-22	24	7.2	8:04	12:06	4:02	7.3	0.08	0.1
05-19-22	24	7.2	8:44	12:56	4:12	7.6	0.08	0.1
05-20-22	24	7.2	8:43	12:50	4:07	7.4	0.08	0.1

210 Flow rates: ¹5 L/min, ²30 L/min, ³28.3 L/min

211

212 2.2 Sampling and instrumentation

213 The simultaneous sampling was performed using, per site, a MiniVol TAS (Tactical Air
 214 Sampler; Airmetrics) with a 2.5 µm cut-size inlet operated at 5 L min⁻¹, an eight stage micro-
 215 orifice uniform deposit impactor (MOUDI 100R; MSP) operated at a 30 L min⁻¹ flow rate to
 216 separate particles as a function of their aerodynamic diameter (cut sizes of 0.18 µm, 0.32 µm,

217 0.56 μm , 1.0 μm , 1.8 μm , 3.2 μm , 5.6 μm and 10 μm), and a single-stage BioStage Quick Take
218 30 cascade impactor for viable particles (SKC Inc. USA) operated at a 28.3 L min^{-1} flow rate.
219 The MOUDI samples, used to evaluate the INP concentrations, were collected one time a day
220 from May 16th to May 20th, 2022, with the sampling times shown in Table 1 (more details are
221 provided in section 2.2.6). The MiniVol samples were collected daily for 24 h on May 12th,
222 May 13th, May 16th, May 17th, May 18th, May 19th and May 20th, 2022, on 47 mm Teflon filters
223 (Pall Science), and were used for the ionic and elemental composition analysis. The BioStage
224 impactor samples with a 10 μm cut-size inlet were used for culturable bacteria and fungi
225 identification. They were collected once a day (at 10:00 am for 5 mins) on the same dates as
226 the MiniVol samples (more details are described in section 2.2.5). The general overview of the
227 sampling campaign is shown in Table 1.

228

229 **2.2.1 Meteorological data**

230 Meteorological variables such as temperature, relative humidity, wind direction, wind speed,
231 and solar radiation were obtained from the meteorological stations (Campbell Scientific) of the
232 Red Universitaria de Observatorios Atmosféricos (RUOA) and the Programa de Estaciones
233 Meteorológicas del Bachillerato Universitario (PEMBU) placed in CU and C5, respectively.
234 Also, back trajectories of the air masses arriving in both sampling sites were obtained using the
235 Hybrid Single-Particle Lagrangian Integrated Trajectory (HYSPLIT) model from the National
236 Oceanic and Atmospheric Administration (NOAA) for 72 h at 250 m a.g.l (Draxler, 2010).

237

238 **2.2.2 Criteria pollutants**

239 The concentrations of O₃, CO, NO_x, and SO₂, were measured with the Teledyne (Sandiego,
240 CA) ultraviolet photometry API Model 400E non-dispersive infrared analyzer, API model
241 300E, and API model 200E, respectively. The PM_{2.5} was measured with a Thermo Scientific
242 (Franklin, MA) tapered element oscillating microbalance (TEOM) Model 1400A ambient
243 particulate monitor at a flow rate of 3 L min^{-1} .

244

245 **2.2.3 PM_{2.5} ionic composition**

246 The ionic composition was obtained using a Dionex ICS-1500 ion chromatography (IC) at the
247 Laboratorio de Aerosoles Atmosféricos of the Institute for Atmospheric Sciences and Climate
248 Change, UNAM. For PM_{2.5} aerosol sample extraction, the MiniVol sample filters (i.e., 47 mm
249 Teflon filters) were submerged in 10 mL of deionized water, sonicated for one hour (using an

250 ultrasonic bath at a temperature below 27 °C), and shaken at 350 rpm for six hours (Sartorius
251 CPA225D).

252

253 Anion analysis was performed using a Dionex IonPac AS23 column (4 × 250 mm) and a
254 carbonate solution (Na₂CO₃ 4.5 mM – NaHCO₃ 0.8 mM) as the mobile phase at a flow rate of
255 1 mL min⁻¹. Three anions (i.e., NO³⁻, SO₄⁻², and Cl⁻) were measured using the described setup.

256 Cation analysis was performed using a Dionex IonPac CS12A column (4 mm × 250 mm) and
257 a methanesulfonic acid (CH₄O₃S 20 mM) with a flow rate of 1 mL min⁻¹ as a mobile phase.

258 Five cations (i.e., Na⁺, K⁺, NH₄⁺, and Ca²⁺) were measured using the described setup. The limits
259 of quantification (LOQ) and determination (LOD) were calculated using the linear regression
260 of standards calibration. More details about IC setup and similar methods can be found in Castro
261 Romero et al. (2024).

262

263 **2.2.4 PM_{2.5} X-ray fluorescence**

264 The elemental composition analysis was performed at the Laboratorio de Aerosoles, Instituto
265 de Física, UNAM following Espinosa et al. (2012). An X-ray fluorescence spectrometer with
266 an Oxford Instruments (Scotts Valley, CA, USA) tube with Rh anode and an Amptek X-
267 123SDD spectrometer (Bedford, MA, USA) was used to obtain the elemental composition of
268 all MiniVol sample filters (i.e., 47 mm Teflon filters). The instrument was operated at 50 kV
269 and a current of 750 μA, irradiating for 900 s per spectrum. More details of instrument
270 calibration can be found at Espinosa et al. (2012). The chemical composition was quantified
271 using the methodology reported by Espinosa et al. (2010). The percentage fraction for each
272 element was determined by using the relationship between the analyzed element concentration
273 and the total mass concentration.

274

275 **2.2.5 Airborne culturable microorganisms' collection and identification**

276 For the microorganism's identification (bacteria and fungi), petri dishes (100 mm × 10 mm)
277 with three different media were used to impact and collect particles of 10 μm or less in size,
278 and grow the microorganisms using the BioStage impactor: trypto-casein soy agar (TSA, BD,
279 Bioxon) supplemented with 100 mg L⁻¹ of cycloheximide (Sigma-Aldrich) (to prevent growth
280 fungal propagules) for mesophilic cultivable bacteria (MCB), Reasoner's 2A (R2A, Condalab)
281 for slow-growing species of MCB, and malt extract agar (MEA, BD Bioxon) for cultivable
282 fungal propagules. The sampling time on the BioStage impactor was set to 5 min.

283

284 The concentrations of cultivable bacteria were reported as Colony Forming Units per m³ of air
285 (CFU m⁻³). The following procedure was applied as described in Melchum et al. (2023). The
286 TSA, R2A, and MEA were cultured at 35 °C, 35 °C, and 25 °C, respectively. After 48 h (for
287 TSA bacteria) and 72 h (for R2A bacteria and fungi), the CFU were quantified, and the Petri
288 dishes were sealed with parafilm and stored at 4 °C for further analysis. Representative bacterial
289 colonies were randomly selected and purified by several reseedings in TSA. Gram staining was
290 performed to classify the bacteria as Gram-positive or Gram-negative by microscopic
291 observation (100×) of the preparations. Isolated bacteria confirmation of identity was
292 performed by mass spectroscopy, using the Microflex MALDI-TOF MS® (Bruker Daltonics,
293 Bremen, Germany). The identification of fungal species was carried out at the genus level using
294 taxonomic keys based on macroscopic colony characteristics and spore microscopic
295 examination (60×) (Rodriguez-Gomez et al., 2020; Melchum et al., 2023).

296

297 **2.2.6 Ice nucleation experiments**

298 The INP concentration of the collected aerosol particles were obtained using a UNAM-Micro-
299 orifice Uniform Deposit Impactor-Droplet Freezing Technique (UNAM-MOUDI-DFT),
300 described in Córdoba et al. (2021) with its main features shown in Fig. S3.

301

302 Aerosol particles were collected on hydrophobic glass coverslips as substrates at 0.56 µm, 1.0
303 µm, 1.8 µm, 3.2 µm, 5.6 µm and 10 µm cut-offs MOUDI stages (flow rate of 30.0 L min⁻¹).
304 After sampling, every substrate was stored in sealed, sterilized Petri dishes at 4 °C until its
305 analysis.

306

307 Each glass coverslip was analyzed using the UNAM-MOUDI-DFT to simulate the immersion
308 freezing mode between 0 °C and -40 °C. For the INP experiments, the glass coverslips were
309 placed on a sample holder inside the cold cell with the sample holder at the top of two blocks
310 for a sample temperature control: a heating block (copper-made block with two heating
311 resistances, 100 W and 120 V) and a cooling block (cooled by refrigerator circulator, PRO-
312 RP1090, LAUDA), with the cold block at the bottom. To induce droplet formation, humid air,
313 carried by nitrogen (grade 4.8, INFRA), is directed toward the sample holder at 0 °C. Once
314 approx. 30-40 droplets of ca. 170 µm radius are formed, a dry airstream is introduced into the
315 cold cell to shrink the droplets, aiming to minimize contact between them. Finally, the cold cell
316 was isolated, and a temperature ramp from 0 °C to -40 °C (at a cooling rate of 10 °C min⁻¹) was
317 run until the freezing of each drop was observed. The entire process was recorded with a video

318 camera (MC500-W, JVLAB) attached to an optical microscope (Axiolab Zeiss, Germany) with
319 a 5×/0.12 magnification objective, the microscope objective being coupled to the sample holder
320 via a glass coverslip at the top of the cold cell.

321

322 From the recorded video, it is possible to determine the freezing temperature for each droplet,
323 which allows calculation of the frozen fraction (F_{ice}) and the INP number concentration as a
324 function of temperature ([INP(T)]). F_{ice} was calculated using Equation 1:

$$325 \quad F_{ice} = \frac{N_{ice}}{N_{ice} + N_{droplets}} \quad (1)$$

326 where N_{ice} and $N_{droplets}$ are the number of frozen droplets (dimensionless) and the number of
327 unfrozen droplets (dimensionless), respectively (Kanji et al., 2017).

328

329 The [INP(T)] was calculated using Equation 2 (Mason et al., 2015; Córdoba et al., 2021):

330

$$331 \quad [INP(T)] = -\ln\left(\frac{N_u(T)}{N_0}\right) \cdot \left(\frac{A_{deposit}}{A_{DFT}V}\right) \cdot N_0 \cdot f_{ne} \cdot f_{nu,0.25-0.10\text{ mm}} \cdot f_{nu,1\text{ mm}} \quad (2)$$

332

333 where $N_u(T)$ is the number of unfrozen droplets at T (°C), N_0 is the total number of droplets
334 (dimensionless), $A_{deposit}$ is the total area of the aerosol particles deposited on the hydrophobic
335 glass coverslip (cm²), A_{DFT} is the area of the sample analyzed by the DFT (cm²), V is the volume
336 of air through the MOUDI (L), f_{ne} is a correction factor to account for the uncertainty associated
337 with the number of nucleation events in each experiment (dimensionless), and f_{nu} is a correction
338 factor to account for changes in particle concentration across each MOUDI sample
339 (dimensionless). Additionally, this equation accounts for the possibility that multiple particles
340 may be present within a droplet (Vali, 1996), the correction for the total area covered by
341 particles deposited on the MOUDI coverslips, and corrections for inhomogeneities in particle
342 deposition. More details of Equation 2 and the applied corrections can be found in Mason et al.
343 (2015).

344

345 **2.2.7 Data analysis**

346 The STATISTICA[®] 12 software (StatSoft, TIBCO Software Inc., USA) was employed to
347 evaluate basic statistics and cluster analysis of data from the different analysis described in
348 section 2.2. With the main objective of identifying associations among chemical species and
349 their possible sources, a cluster analysis using Ward's method of amalgamation and Pearson
350 correlation coefficients was carried out to construct dendrograms for both sampling sites.

351

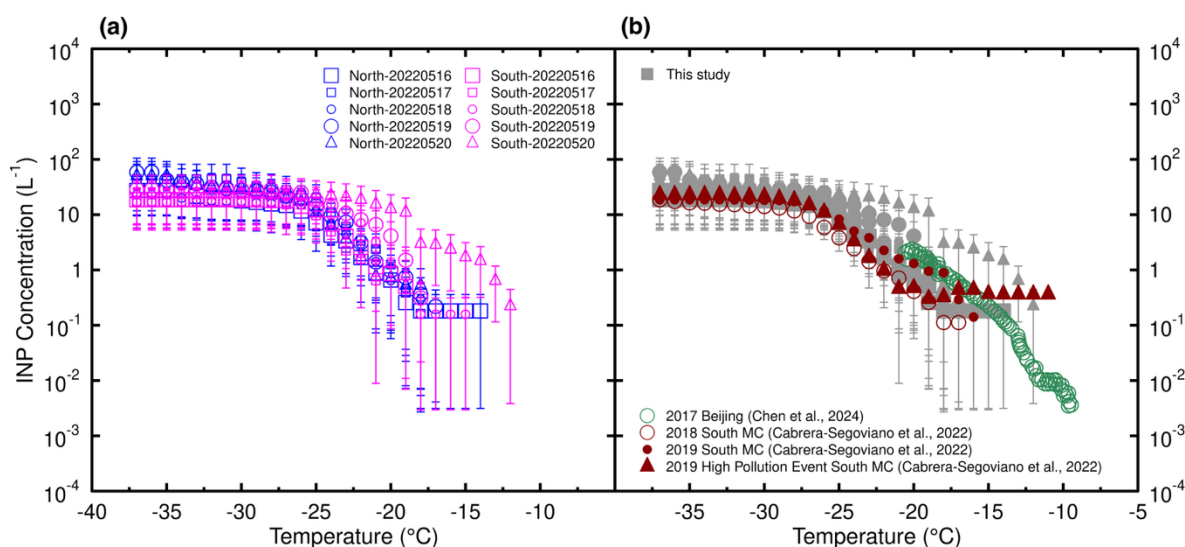
352 **3. Results and Discussion**

353 **3.1 Frozen fraction and INP concentration variability**

354 Following the procedure described in section 2.2.6, the frozen fraction and the INP
355 concentrations were obtained for each sample from May 16th to 20th. Figure S4 shows the frozen
356 fraction (FF) as a function of particle size (aerodynamic diameters of 0.56 μm to 10 μm) for
357 the northern and the southern sampling sites. This size range was selected considering that
358 super-micron particles contribute more than 70 % to the total INP population (e.g., Mason et
359 al., 2016; Córdoba et al., 2021). Aerosol particles collected in the present study were able to
360 nucleate ice at temperatures warmer than those required to freeze supercooled liquid drops (i.e.,
361 homogeneous freezing, black line). The homogeneous freezing line was determined using the
362 same procedure described in section 2.2.6 with a brand-new substrate (i.e., without aerosol
363 particles impacted on them). The FF curve of the homogeneous freezing experiments is
364 comparable with other data for supercooled liquid drops such as the 100 μm and $89 \pm 7 \mu\text{m}$
365 liquid water drops reported by Shardt et al. (2022) and Tarn et al. (2021), respectively.

366

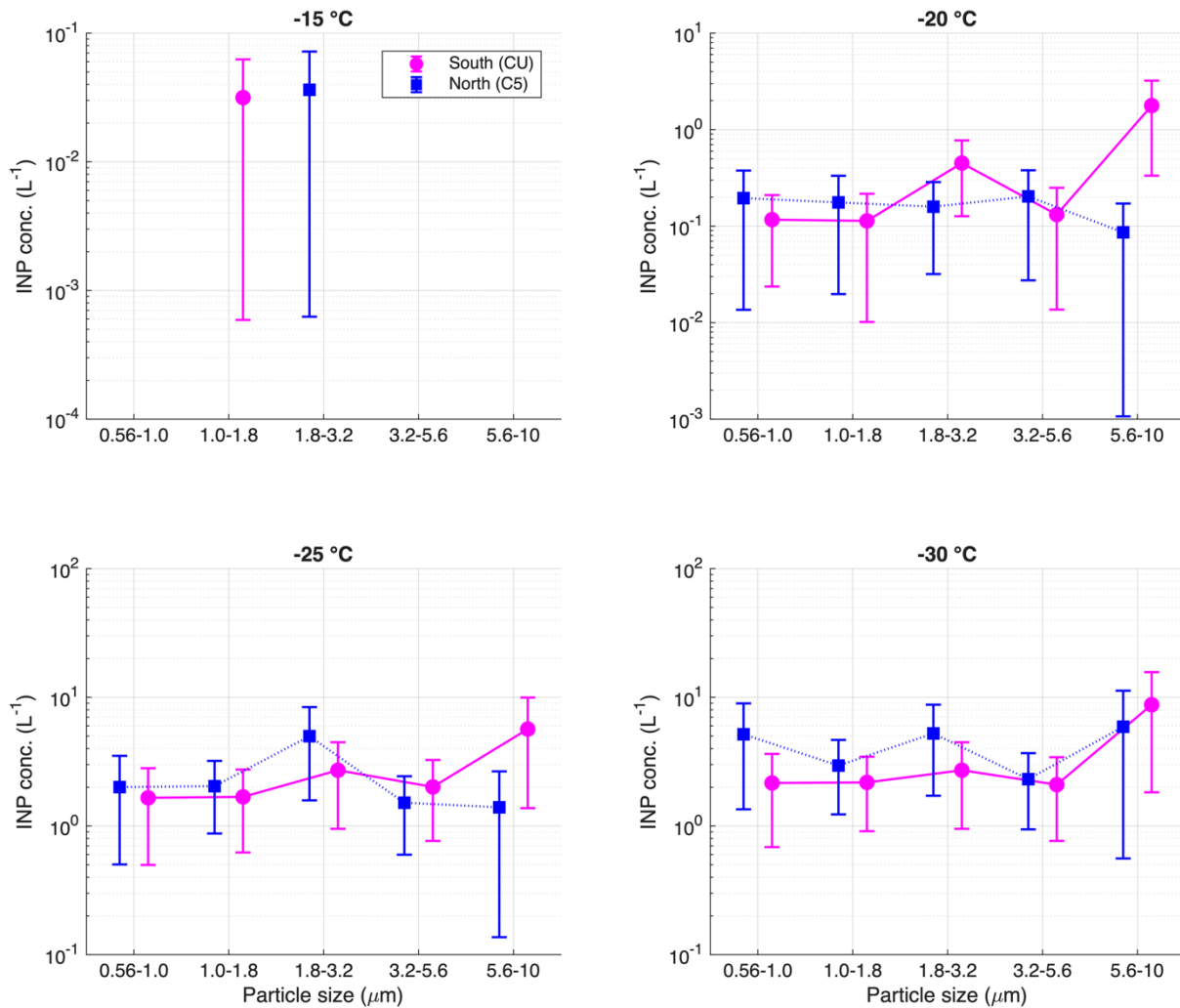
367 The total INP concentrations (i.e., the accumulated INP concentration, represented by the sum
368 of each MOUDI stage INP concentration for each sample) at both sites are shown in Fig. 2.
369 Although the INP concentrations measured at both sites were comparable, the exemption was
370 the May 20th sample (Fig. 2a), where higher and statistically significant differences in INP
371 concentrations were measured in the southern site between -19 °C and -22 °C (considering the
372 Agresti and Coull (1998) method to calculate 95 % confidence intervals). Figure 2b also
373 indicates that the INP concentrations from the present study agree well with those reported by
374 Cabrera-Segoviano et al. (2022) for Mexico City and by Chen et al. (2024) for Beijing (between
375 -19 °C and -22 °C), a polluted megacity such as the MCMA.



376
 377 Figure 2. INP concentration as a function of temperature for (a) the measurements performed
 378 between May 16th and 20th, 2022 at the northern and southern site of the MCMA, and (b)
 379 literature measurements for the MCMA (2018 and 2019), and Beijing (2017) reported by
 380 Cabrera-Segoviano et al. (2022) and Chen et al. (2024), respectively. The dark red triangles in
 381 (b) panel represent the INP concentration values reported for 2019 High Pollution Event at
 382 South MC (Cabrera-Segoviano et al., 2022). The error bars represent the carried experimental
 383 uncertainty calculated using the method described in Mason et al. (2015).

384
 385 The impact of particle size on the frozen fraction at both sampling sites does not show a clear
 386 trend (Fig. S4). Likewise, Fig. 3 shows that the mean INP concentration (which represents the
 387 average of all samples for each MOUDI stage) measured on urban particles from the MCMA
 388 is not clearly size-dependent. In theory, particle size and INP efficiency are related. This
 389 relationship is attributed to surface active sites, as larger particles contain a higher concentration
 390 of active sites (Vali, 1996; Hoose and Möhler, 2012; Kanji et al., 2017); however, as urban
 391 ambient samples are a complex mixture of particles with different compositions, the
 392 relationship between particle size and INP is not straightforward as it requires deeper chemical
 393 analysis to understand the heterogeneity in particles chemical composition on each MOUDI stage.
 394
 395 Even though the particle size did not show a trend, a clear difference is observed at larger
 396 particle sizes (i.e., particles between 5.6-10 μm) between the two sampling sites. Showing that
 397 the contribution from larger particles to the INP concentrations was found to be greater in the
 398 south of the MCMA. Although there is no chemical composition information available for these

399 large particles, we encourage future studies to help understating the importance of PM₁₀
 400 particles.



401
 402 Figure 3. INP average concentration as a function of particle size at -15 °C, -20 °C, -25 °C, and
 403 -30 °C, for southern (CU, magenta) and northern (C5, blue) MCMA. The error bars represent
 404 the carried experimental uncertainty calculated using the method described by Mason et al.
 405 (2015).

406
 407 **3.2 Ice nucleation activity vs. criteria pollutants**

408 Time series of five criteria pollutant concentrations at both sites are shown in Fig. S2. PM_{2.5}
 409 concentration was found to be comparable at both sites, with a slight increase along the last part
 410 of the campaign. The maximum difference in PM_{2.5} concentration between both sites was 6.60
 411 μg m⁻³. Although high hourly values of PM_{2.5} were measured (in the order of ~60 μg m⁻³), they
 412 cannot be considered as *high pollution episodes* as was the case described in Cabrera-Segoviano
 413 et al. (2022) where PM_{2.5} concentrations above 80 μg m⁻³ were measured (Carabali et al., 2021).
 414 Similar to previous studies performed within the MCMA, CO, SO₂, and NO_x concentrations

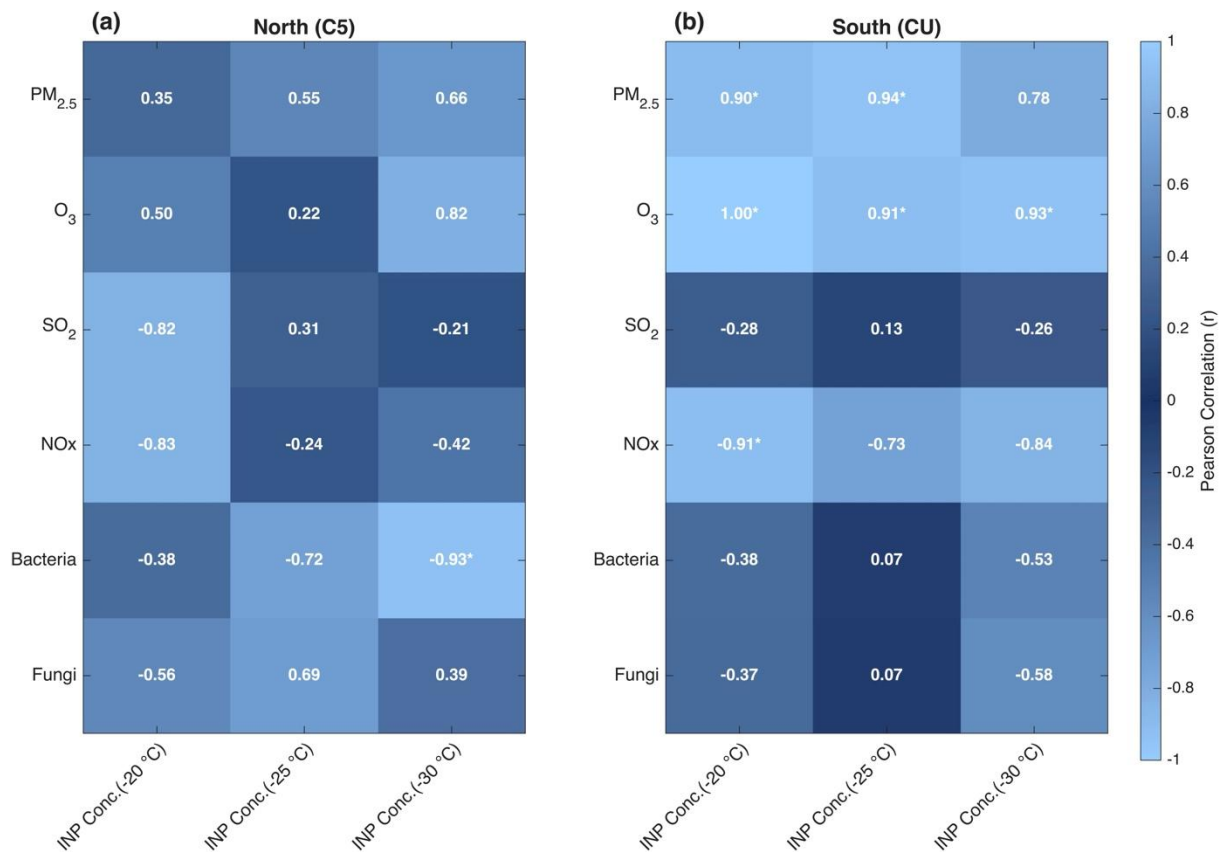
415 were higher at the northern site, with 0.6 ppm, 14 ppm, and 60 ppm maximum difference
416 between the northern and southern sites for CO, SO₂, and NO_x, respectively (Fig. S2). This
417 behavior is related to local emissions, such as gasoline-fueled vehicular emissions and industrial
418 activity (Vega et al., 2004; Castro et al., 2024).

419
420 O₃ concentrations were higher at the southern site (i.e., a 30 ppm maximum difference between
421 both sites). Local emissions from vegetation cover prevalent in southern MCMA, such as
422 volatile organic compounds (VOCs), together with local NO_x emissions and transport can
423 explain the O₃ behavior. It is well known that VOCs may participate in O₃ production by
424 photochemistry and lead to higher concentrations (Pinto et al., 2010; Amador-Muñoz et al.,
425 2016). Therefore, the southern site is likely enriched in biogenic secondary organic aerosols
426 (SOA) compared to the northern site (Aiken et al., 2009; Cooke et al., 2024), with unknown
427 implications in the INP population.

428
429 The INP concentrations shown in Fig. 2 were comparable at colder temperatures, with a slightly
430 higher concentration at the southern site observed on the last sampling day at warm
431 temperatures. Given that a slight increase in PM_{2.5} concentration was also observed on May
432 20th at the southern site (Fig. S2), there may be a small relationship between INP concentration
433 at warm temperatures and PM_{2.5}. Figure 4 shows the calculated Pearson correlation coefficients
434 between the measured criteria pollutants and INP concentration at -20 °C, -25 °C, and -30 °C
435 for both sampling sites (for particles ranging between 0.56 μm and 3.2 μm). Mean criteria
436 pollutant concentrations between 08:00 h and 13:00 h local time were used to match the INP
437 sampling periods. Figure 4 shows high correlations between PM_{2.5}, O₃, and the INP parameters
438 at the southern site, implying that both pollutants can impact the physicochemical properties of
439 the INP population at this site. On the other hand, no significant correlations were found at the
440 northern site. As the INP sizes in both sites are identical, the observed differences are likely
441 linked with differences in the PM_{2.5} composition. As shown in Figs. 5 and S5, the PM_{2.5}
442 elemental and ionic composition in the northern and southern sites have important differences.
443 As the composition is clearly different, the interaction between fine particles, and hence INPs,
444 with O₃ is expected to differ in both sites as well. As the PM_{2.5} sampling time was much larger
445 (24 h) than the 4 h INP sampling, a direct correlation between the elemental and ionic
446 composition with the INP concentrations was not assessed.

447

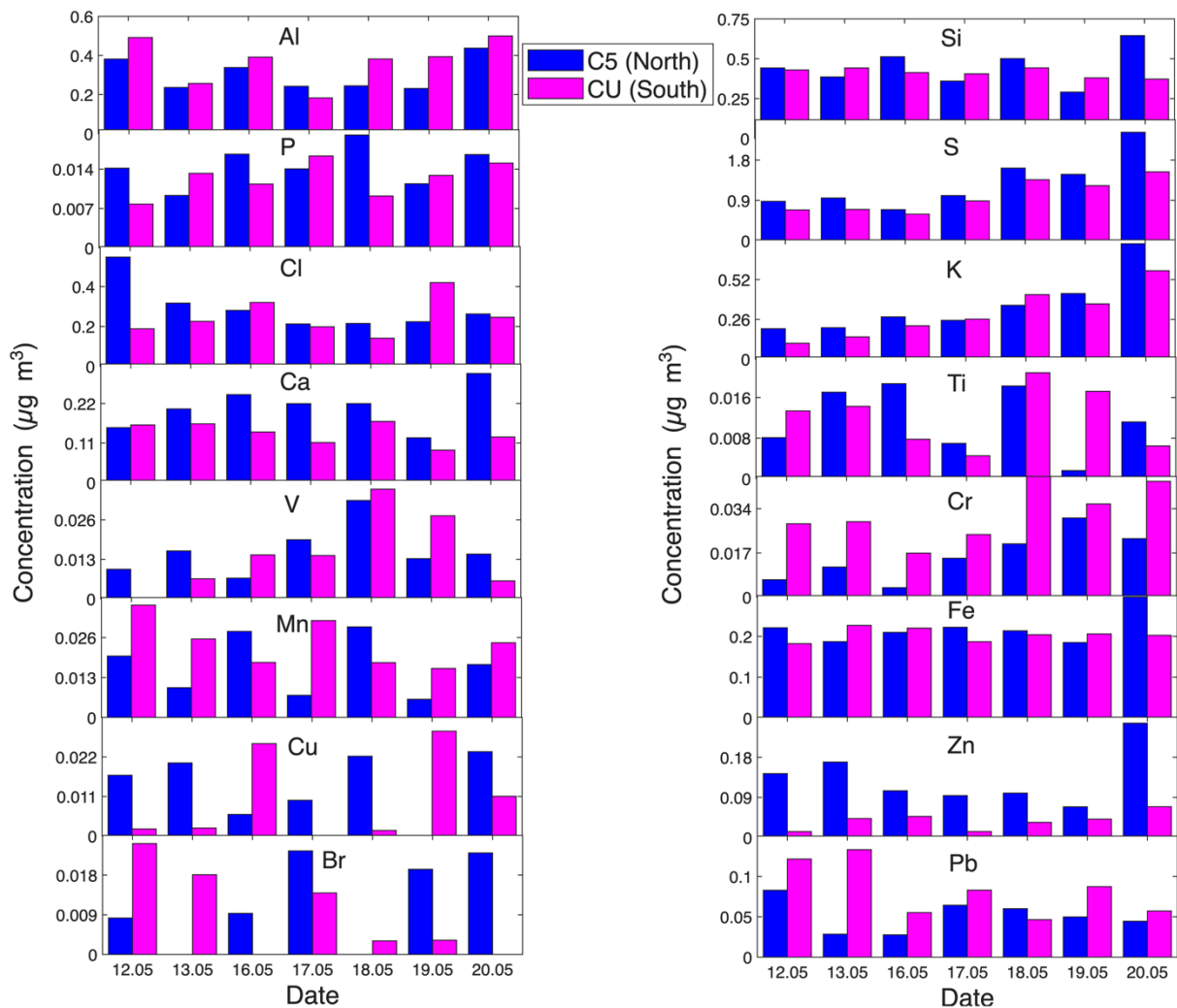
448 This suggest that different sources of particles could be present at both MCMA sites, but no
 449 correlation was found that anthropogenic pollution could modify INP concentration. The
 450 relationship between PM_{2.5} and INP concentrations has been previously evaluated (Chen et al.,
 451 2018; Bi et al., 2019; Córdoba et al., 2021; Cabrera-Segoviano et al., 2022), with highly
 452 contrasting results, but showing that urban particle concentrations alone do not affect INP
 453 concentration.
 454



455
 456 Figure 4. Heat map with the Pearson correlation coefficients (r) for the relationships between
 457 the INP parameters (i.e., INP concentrations at -20 °C, -25 °C and -30 °C) and the ambient
 458 criteria pollutants concentrations (i.e., PM_{2.5}, O₃, NOx, and SO₂) for (a) northern (C5) site and
 459 (b) southern (CU) site of the MCMA. Correlation analysis between CO and INP parameters
 460 was excluded due to the unavailability of CO data for most INP sampling days. The statistically
 461 significant coefficients (with 95 % confidence level) are marked with an asterisk.
 462

463 The analysis of the elemental composition indicates that the concentration of 12 of the 16
 464 analyzed elements (i.e., Si, P, S, Cl, K, Ca, Ti, V, Fe, Cu, Zn, and Br) was higher at the northern
 465 site as shown in Fig. 5. The maximum measured concentrations were reported for Al and Si, an
 466 indication of the presence of aluminum silicates from resuspended dust, as previously reported

467 (Querol et al., 2019; Córdoba et al., 2021). Pb was present at both sampling sites with a
 468 maximum concentration of $0.13 \mu\text{g m}^{-3}$ and $0.08 \mu\text{g m}^{-3}$ for CU and C5, respectively. The Pb
 469 sources are typically linked with local industrial activities and the usage of low quality fuels
 470 (Moreno et al., 2008; Hernández-López et al., 2020). The World Health Organization (WHO)
 471 recommends an annual average airborne Pb concentration of $0.5 \mu\text{g m}^{-3}$ as part of its Global
 472 Air Quality Guidelines; therefore, the values reported in this work did not exceed this limit.
 473



474
 475 Figure 5. Concentration of the different individual elements analyzed by XRF on $\text{PM}_{2.5}$ at the
 476 northern (C5, blue) and southern (CU, magenta) sites.

477
 478 The maximum S concentration (i.e., $2.42 \mu\text{g m}^{-3}$) observed in C5 is lower than the values
 479 reported in previous studies ($3.24 \mu\text{g m}^{-3}$, Castro et al., 2024; $3.38 \mu\text{g m}^{-3}$, IMADA, 1997; 5.10
 480 $\mu\text{g m}^{-3}$, Vega et al., 2004), likely related to differences in the sampling month, but higher than
 481 the highest S concentration reported in CU (i.e., $1.54 \mu\text{g m}^{-3}$). S and K are markers of high-
 482 pollution events in megacities, typically linked with industrial activity, gasoline combustion,

483 and BB emissions (Ríos and Raga, 2018; Raga et al., 2021). In this study, a rise in S and K
484 concentrations during the last sampling day (i.e., May 20th) is clearly observed (Figs. 5 and S5)
485 and could be attributed to local and regional BB.

486

487 To further explore the chemical composition of urban aerosol particles at both sampling sites,
488 the ion composition was analyzed. Figure S5 reinforces the significant differences in the urban
489 particles' chemical composition between the two microclimates. The five analyzed cations
490 (Na^+ , K^+ , Ca^{2+} , NH_4^+ , and Mg^{2+}) and the three analyzed anions (Cl^- , NO_3^- , and SO_4^{2-}) showed
491 higher concentrations at the northern site. The relationships among SO_4^{2-} , NO_3^- , and NH_4^+ at
492 both sampling sites are shown in Tables S3 and S4. The strong observed correlation suggests
493 the presence of $(\text{NH}_4)_2\text{SO}_4$ and NH_4NO_3 at both sites, two compounds produced by
494 photochemical reactions driven by gasoline and diesel emissions (Vega et al., 2004; Hernández-
495 López et al., 2020; Castro Romero et al., 2024).

496

497 Figure S6 shows that the HYSPLIT backward trajectories at 250 m AGL at both MCMA sites
498 overlaid on the NASA FIRMS real-time active fire locations for the sampling period (i.e., May
499 12th to May 20th, 2022). Even though not all backward trajectories pass through active fires, the
500 overlap between some back-trajectories and active fires suggests that the local and regional
501 transport of BB particles could contribute to the observed differences in the chemical
502 composition, as shown elsewhere (e.g., Carabali et al., 2021). Additionally, Fig. S6 shows that
503 air-masses in both sampling sites came from very similar directions during the sampling period,
504 so particle transport between two sites cannot be neglected at all.

505

506 To evaluate potential sources of the measured urban aerosol particles, a cluster analysis was
507 applied using all the chemical species to generate a dendrogram for each sampling site.
508 Hierarchical clustering was conducted using Ward's method, with Pearson correlation
509 coefficients employed as the similarity measure. This technique groups variables by minimizing
510 increases in within-cluster variance, leading to clusters of species with similar temporal
511 patterns. The resulting dendrogram illustrates the level of similarity among variables, where
512 shorter linkage distances represent stronger relationships. Principal cluster components can be
513 linked to a potential source as shown in previous literature analysis of similar samples
514 (Reynoso-Cruces et al., 2023). The dendrogram for the southern site (Fig. S7) presents three
515 groups: the orange cluster with anthropogenic oxidized and non-oxidized species and a
516 contribution of BB regional emissions; the green cluster with geogenic oxidized and non-

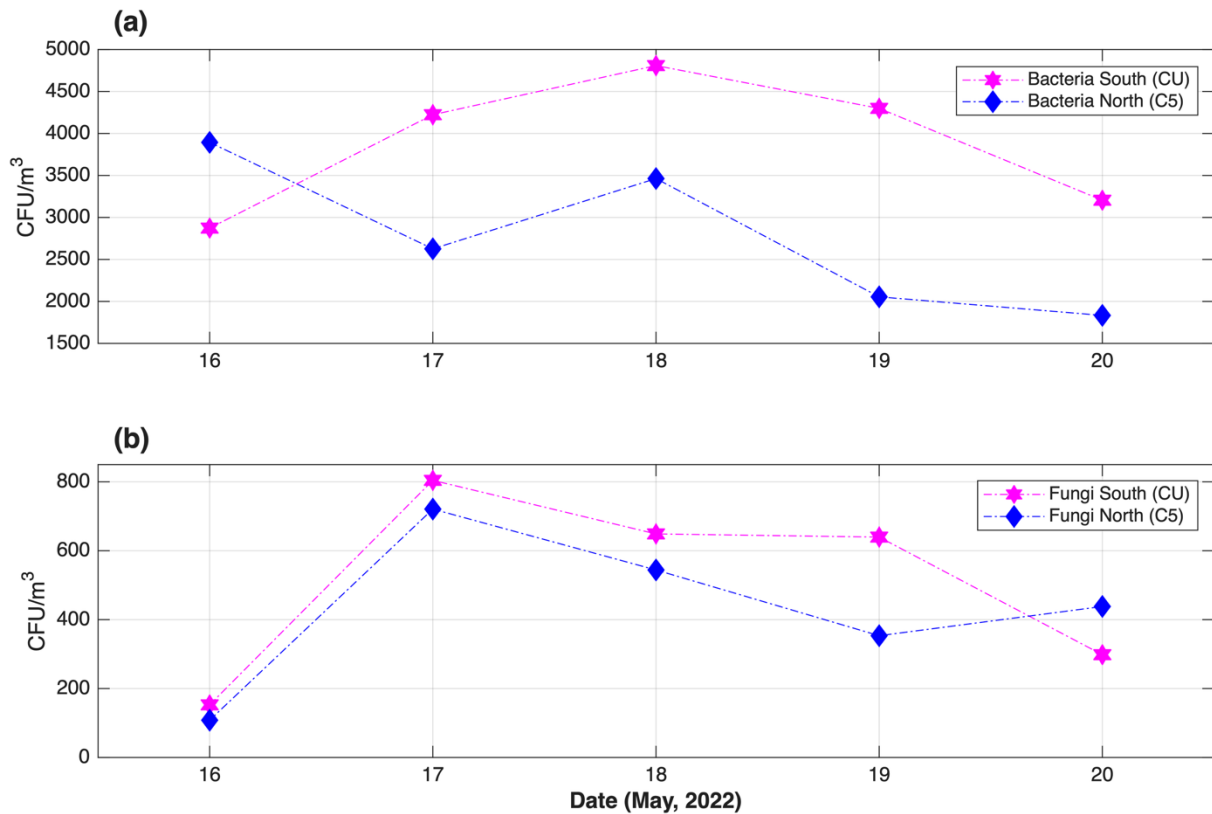
517 oxidized species; and the brown cluster with resuspended soil originated from rural areas with
518 geogenic species and some anthropogenic contributions. Likewise, the dendrogram for the
519 northern site (Fig. S8) also shows three groups: the orange cluster, which corresponds to
520 anthropogenic oxidized and non-oxidized species; the blue cluster, containing mostly
521 anthropogenic oxidized species from fossil fuels; and the brown cluster with oxidized and non-
522 oxidized resuspended soils. This cluster analysis highlights the effects of land use and BB on
523 the chemical composition of the urban particles across these two microclimates of the MCMA
524 and denotes sample complexity.

525

526 **3.3 Ice nucleation activity vs. culturable microorganisms**

527 To assess the presence of biological particles at both sampling sites, the concentrations of
528 culturable bacteria and fungi were measured in parallel to the INPs. Significant daily variations
529 in bacteria and fungi concentrations at both sampling sites were observed, as shown in Fig. 6.
530 The measured CFU m⁻³ follow the same pattern at both sites, an inverse pattern with PM_{2.5}
531 concentration. The average concentrations of bacteria and fungi at the northern site were 2774
532 CFU m⁻³ and 433 CFU m⁻³, respectively; at the southern site, the average concentrations of
533 bacteria and fungi were 3882 CFU m⁻³ and 509 CFU m⁻³, respectively. The average bacteria
534 concentrations reported in this study are higher than those reported for Yucatán, México (i.e.,
535 69 CFU m⁻³) (Rodriguez-Gomez et al., 2020), Tijuana, México (i.e., 340 CFU m⁻³) (Hurtado et
536 al., 2014), northwestern Amazon, Colombia (i.e., 228 CFU m⁻³) (Russy-Velandia et al., 2025),
537 and Qingdao, China (i.e., 83 CFU m⁻³) (Li et al., 2011). In contrast, the average fungi
538 concentrations reported in this work are lower than those reported for Yucatán, México (i.e.,
539 1018 CFU m⁻³) (Rodriguez-Gómez et al., 2020), and are consistent with the results reported for
540 northwestern Amazon, Colombia (i.e., 642 CFU m⁻³) (Russy-Velandia et al., 2025) and
541 Qingdao, China (i.e., ~300 CFU m⁻³) (Li et al., 2011). Consistent with the aforementioned
542 studies, the Gram staining analysis indicated that 57 % of the culturable bacteria were Gram-
543 positive

544



545
 546 Figure 6. Time series of the concentration (CFU/m³) of total mesophilic **a)** bacteria and **b)** fungi
 547 measured in the northern (C5, blue) and southern (CU, magenta) sites.

548
 549 A total of 21 bacterial species and eight fungal genera were identified between both sampling
 550 sites (Tables S5 and S6). Although bioparticles were clearly present at both sites, it is doubtful
 551 that they played a key role in the ice nucleating abilities of the collected urban particles. The
 552 FF reported in this work differ significantly with those reported for bioaerosols, typically
 553 showing activation close to -10 °C (Hoose et al., 2010; Knopf et al., 2011; Wex et al., 2015;
 554 Kunert et al., 2019). It is still possible that INP contributed by bioparticles are below the
 555 detection limit of our setup because of sampling methods (i.e., differences in cut-off and total
 556 sampling time). However, an overview of INP concentrations observed in the atmosphere by
 557 Petters and Wright, (2015) indicates that our detection limit of 0.1 L⁻¹ is high enough to enable
 558 the detection of biological particles if they were present. Although the northern site showed
 559 relative higher, but not significant, correlations between microorganisms' concentration and
 560 INP concentrations (Fig. 4), all INP analysis indicate that the identified culturable
 561 microorganisms did not play a primary role in the measured INP concentration of the MCMA
 562 samples. Moreover, the sampling season (dry vegetation season) may be governing the
 563 relationship between biological particles and INP concentration reported here, making it

564 necessary to assess INP concentrations at different times of year (i.e., across meteorological
565 seasons).

566

567 Although some of the identified bacteria and fungi genera and species have been reported to
568 act as INPs at warm temperatures (Tables S5 and S6), it is completely unknown if the MCMA
569 microorganisms contained the INA protein. Melchum et al. (2023) showed that among the 64
570 analyzed species, the most efficient INP was the *Cupriavidus pauculus* bacteria, with an onset
571 freezing temperature of -11.8 °C. Therefore, as demonstrated by Melchum et al. (2023) and
572 previously by Schnell and Vali (1976), tropical biological particles appear to be inefficient
573 INPs. The behavior of bacterial and fungal concentration between the northern and southern
574 sites were evaluated by the Pearson correlation analysis shown in Tables S7 and S8. As
575 expected, mixed values of Pearson coefficients reflect that not all bacteria and fungi found at
576 the southern site (closed to vegetated areas) are present in the northern site.

577

578

579 **4. Conclusions**

580 This work evaluated, for the first time, simultaneous measurements of INP concentration at two
581 sites within one of the largest megacities worldwide. Aerosol particles sampled in the southern
582 and northern parts of the MCMA acted as INPs, via immersion freezing. The average INP
583 concentrations varied between $(0.04 \pm 0.04) \text{ L}^{-1}$ and $(24.9 \pm 18) \text{ L}^{-1}$ at temperatures between -
584 15 °C and -30 °C. The measured INP concentrations agree with those from previous studies
585 conducted in Mexico City (Mexico) and Beijing (China), showing that INP concentrations are
586 not affected by anthropogenic emissions but are indeed influenced by soil use and other local
587 sources. Although earlier studies have shown that particle size plays a role in the INP
588 concentration of Arctic, urban, marine, biomass burning, and mineral dust particles (e.g., Mason
589 et al., 2016; Córdoba et al, 2020), the present results showed that the INP concentration of
590 complex urban particles from the MCMA are not strongly size-dependent (see Figs. S4 and 3).

591

592 The present results clearly demonstrated the existence of microclimates within the MCMA. The
593 INP parameters of the MCMA urban particles correlated with $\text{PM}_{2.5}$ and O_3 , at the southern
594 site, corroborating that particle mass concentration and ozone concentration are very important
595 for the southern MCMA microclimate. Nevertheless, urban aerosol particles show similar INP
596 concentrations across both sites, suggesting that INP activity does not depend on a specific
597 aerosol type, but rather on the bulk complex mixture of aerosol particles or on the dominance

598 of long-range-transported INPs, with no or only a few additional urban sources. Local emissions
599 and the regional transport of different particles (e.g., BB, biogenic SOA, anthropogenic SOA,
600 mineral dust particles, and bioaerosol), are highlighted as the primary sources of urban aerosol
601 particles along the MCMA. These results are consistent with previous studies in the MCMA
602 that have mostly focused on aerosol chemical composition (Molina et al., 2010; Amador-
603 Muñoz et al., 2011; Ladino et al., 2018).

604

605 Although the distance between both sampling sites is just 16 km, aerosol sources and
606 atmospheric processes linked to particle formation and aerosol aging (e.g., gas-to-particle
607 conversion, organic coatings, and photochemistry) are quite different. This implies key local
608 implications in particle characteristics (i.e., chemical composition, particle morphology, and
609 particle size) that could impact the INP concentration. The present study demonstrates that a
610 larger contribution of unknown large urban aerosol particles (i.e., particles between 5.6-10 μm)
611 could be important for heterogeneous MPC formation at the southern MCMA site, as evidenced
612 by the rise in INP concentration at $-20\text{ }^{\circ}\text{C}$ (see Figs. 2 and 3). Therefore, if we aim to improve
613 the current understanding of aerosol-cloud interactions above this megacity, it is crucial to
614 consider the different microclimates to avoid assuming that aerosol physicochemical and
615 biological characteristics within the megacity are homogeneous. Thus, differences in the local
616 anthropogenic activities, biogenic emissions, population density, and land use are key drivers
617 that must be considered.

618

619 Although the present work shows that air pollutants such as $\text{PM}_{2.5}$ and ozone can be linked with
620 the ice nucleating abilities of urban aerosol particles, it is important to understand the role and
621 the origin of the super-micron particles as they are a large contributor to the MCMA INP
622 population.

623

624

625 **Author contributions.** KV, DR, JAC, FC, and LAL performed the field measurements. KV,
626 DR, JAC, FC, SMT, and LAL analyzed the data. GBR and LAL designed the field campaigns
627 and were responsible for funding acquisition. KV, SMT, and EN conducted the INP analysis.
628 OR supported the field campaigns and data acquisition. HA conducted the ionic composition
629 analysis. JM conducted the X-ray fluorescence chemical analysis. JAC, IR, LM, and ES
630 conducted the microorganism's identification analysis. SMT and LAL wrote the paper,
631 addressed the reviews and editing, with contributions from all coauthors.

632

633 **Competing interests.** At least one of authors is part of the Editorial board.

634

635 **Acknowledgments.** The authors thank Alison Ruiz, Maria Isabel Saavedra, Juan Carlos Pineda,
636 and Manuel García for their invaluable help. We thank Miguel Sanchez from the Mexico City
637 Atmospheric Monitoring System for sharing the criteria pollutants data and for his support in
638 using their infrastructure. We also thank the RUOA and PEMBU for sharing their
639 meteorological data. Finally, we thank the NOAA for facilitating the use of the surface maps
640 and HYSPLIT.

641

642 **Financial support.** This research was financially supported by the Consejo Nacional de
643 Humanidades, Ciencia y Tecnología (grant no. 1024827) and the Marcos Moshinsky
644 Foundation. Sebastian Mendoza-Téllez thanks SECIHTI for his PhD fellowship.

645

646 **Data availability.** Data will be made available on request.

647

648 **References**

649 Agresti, A. and Coull, B. A.: Approximate is Better than “Exact” for Interval Estimation of
650 Binomial Proportions, *Am. Stat.*, 52, 119–126,
651 <https://doi.org/10.1080/00031305.1998.10480550>, 1998.

652 Aiken, A. C., Salcedo, D., Cubison, M. J., Huffman, J. A., DeCarlo, P. F., Ulbrich, I. M.,
653 Docherty, K. S., Sueper, D., Kimmel, J. R., Worsnop, D. R., Trimborn, A., Northway, M.,
654 Stone, E. A., Schauer, J. J., Volkamer, R. M., Fortner, E., de Foy, B., Wang, J., Laskin, A.,
655 Shutthanandan, V., Zheng, J., Zhang, R., Gaffney, J., Marley, N. A., Paredes-Miranda, G.,
656 Arnott, W. P., Molina, L. T., Sosa, G., and Jimenez, J. L.: Mexico City aerosol analysis during
657 MILAGRO using high resolution aerosol mass spectrometry at the urban supersite (T0) – Part
658 1: Fine particle composition and organic source apportionment, *Atmos Chem Phys*,
659 <https://doi.org/10.5194/acp-9-6633-2009>, 2009.

660 Aldape, F., Flores M., J., Diaz, R. V., Morales, J. R., Cahill, T. A., and Saravia, L.: Seasonal
661 study of the composition of atmospheric aerosols in Mexico City, *Int. J. PIXE*, 01, 355–371,
662 <https://doi.org/10.1142/S012908359100024X>, 1991.

663 Amador-Muñoz, O., Villalobos-Pietrini, R., Miranda, J., and Vera-Avila, L. E.: Organic
664 compounds of PM_{2.5} in Mexico Valley: Spatial and temporal patterns, behavior and sources,
665 *Sci. Total Environ.*, 409, 1453–1465, <https://doi.org/10.1016/j.scitotenv.2010.11.026>, 2011.

666 Amador-Muñoz, O., Bazán-Torija, S., Villa-Ferreira, S. A., Villalobos-Pietrini, R., Bravo-
667 Cabrera, J. L., Munive-Colín, Z., Hernández-Mena, L., Saldarriaga-Noreña, H., and Murillo-
668 Tovar, M. A.: Opposing seasonal trends for polycyclic aromatic hydrocarbons and PM₁₀:

- 669 Health risk and sources in southwest Mexico City, *Atmospheric Res.*, 122, 199–212,
670 <https://doi.org/10.1016/j.atmosres.2012.10.003>, 2013.
- 671 Amador-Muñoz, O., Misztal, P. K., Weber, R., Worton, D. R., Zhang, H., Drozd, G., and
672 Goldstein, A. H.: Sensitive detection of *n*-alkanes using a mixed ionization mode proton-
673 transfer-reaction mass spectrometer, *Atmospheric Meas. Tech.*, 9, 5315–5329,
674 <https://doi.org/10.5194/amt-9-5315-2016>, 2016.
- 675 Behzadi, F., Wasti, A., Haque Rahat, S., Tracy, J. N., and Ray, P. A.: Analysis of the climate
676 change signal in Mexico City given disagreeing data sources and scattered projections, *J.*
677 *Hydrol. Reg. Stud.*, 27, 100662, <https://doi.org/10.1016/j.ejrh.2019.100662>, 2020.
- 678 Bi, K., McMeeking, G. R., Ding, D. P., Levin, E. J. T., DeMott, P. J., Zhao, D. L., Wang, F.,
679 Liu, Q., Tian, P., Ma, X. C., Chen, Y. B., Huang, M. Y., Zhang, H. L., Gordon, T. D., and Chen,
680 P.: Measurements of Ice Nucleating Particles in Beijing, China, *J. Geophys. Res. Atmospheres*,
681 124, 8065–8075, <https://doi.org/10.1029/2019JD030609>, 2019.
- 682 Burrows, S. M., McCluskey, C. S., Cornwell, G., Steinke, I., Zhang, K., Zhao, B., Zawadowicz,
683 M., Raman, A., Kulkarni, G., China, S., Zelenyuk, A., and DeMott, P. J.: Ice-Nucleating
684 Particles That Impact Clouds and Climate: Observational and Modeling Research Needs, *Rev.*
685 *Geophys.*, 60, e2021RG000745, <https://doi.org/10.1029/2021RG000745>, 2022.
- 686 Cabrera-Segoviano, D., Pereira, D. L., Rodriguez, C., Raga, G. B., Miranda, J., Alvarez-Ospina,
687 H., and Ladino, L. A.: Inter-annual variability of ice nucleating particles in Mexico City, *Atmos.*
688 *Environ.*, 273, 118964, <https://doi.org/10.1016/j.atmosenv.2022.118964>, 2022.
- 689 Carabali, G., Villanueva-Macias, J., Ladino, L. A., Álvarez-Ospina, H., Raga, G. B., Andraca-
690 Ayala, G., Miranda, J., Grutter, M., Silva, Ma. M., and Riveros-Rosas, D.: Characterization of
691 aerosol particles during a high pollution episode over Mexico City, *Sci. Rep.*, 11, 22533,
692 <https://doi.org/10.1038/s41598-021-01873-4>, 2021.
- 693 Castro Romero, T., Peralta, O., Prieto, C., Santiago, N., Alvarez-Ospina, H., García Martínez,
694 R., Saavedra Rosado, I., Espinosa Fuentes, M. D. L. L., Hernández, E., Miranda, J., Gómez, V.,
695 Solís, C., Salcedo, D., Torres-Jardón, R., Martínez-Arroyo, A., Ortíz Álvarez, A., Ruíz-
696 Suárez, G., and Ortiz, E.: Characterization of PM_{2.5} during ACU15 campaign in Mexico City,
697 *Geofísica Int.*, 63, 1225–1238, <https://doi.org/10.22201/igeof.2954436xe.2024.63.4.1745>,
698 2024.
- 699 Celada-Murillo, A.-T., Carreón-Sierra, S., Salcido, A., Castro, T., Peralta, O., and Georgiadis,
700 T.: Main Characteristics of Mexico City Local Wind Events during the MILAGRO 2006
701 Campaign within a Meso- β Scale Lattice Wind Modeling Approach, *ISRN Meteorol.*, 2013,
702 1–14, <https://doi.org/10.1155/2013/605210>, 2013.
- 703 Chen, J., Wu, Z., Augustin-Bauditz, S., Grawe, S., Hartmann, M., Pei, X., Liu, Z., Ji, D., and
704 Wex, H.: Ice-nucleating particle concentrations unaffected by urban air pollution in Beijing,
705 China, *Atmospheric Chem. Phys.*, 18, 3523–3539, <https://doi.org/10.5194/acp-18-3523-2018>,
706 2018.
- 707 Chen, J., Wu, Z., Gong, X., Qiu, Y., Chen, S., Zeng, L., and Hu, M.: Anthropogenic Dust as a
708 Significant Source of Ice-Nucleating Particles in the Urban Environment, *Earths Future*, 12,
709 e2023EF003738, <https://doi.org/10.1029/2023EF003738>, 2024.

- 710 Cooke, M. E., Waters, C. M., Asare, J. Y., Mirrielees, J. A., Holen, A. L., Frauenheim, M. P.,
711 Zhang, Z., Gold, A., Pratt, K. A., Surratt, J. D., Ladino, L. A., and Ault, A. P.: Atmospheric
712 Aerosol Sulfur Distribution and Speciation in Mexico City: Sulfate, Organosulfates, and
713 Isoprene-Derived Secondary Organic Aerosol from Low NO Pathways, *ACS EST Air*, 1, 1037–
714 1052, <https://doi.org/10.1021/acsestair.4c00048>, 2024.
- 715 Córdoba, F., Ramírez-Romero, C., Cabrera, D., Raga, G. B., Miranda, J., Alvarez-Ospina, H.,
716 Rosas, D., Figueroa, B., Kim, J. S., Yakobi-Hancock, J., Amador, T., Gutierrez, W., García,
717 M., Bertram, A. K., Baumgardner, D., and Ladino, L. A.: Measurement report: Ice nucleating
718 abilities of biomass burning, African dust, and sea spray aerosol particles over the Yucatán
719 Peninsula, *Atmospheric Chem. Phys.*, 21, 4453–4470, [https://doi.org/10.5194/acp-21-4453-](https://doi.org/10.5194/acp-21-4453-2021)
720 2021, 2021.
- 721 Doran, J. C., Arnott, W. P., Barnard, J. C., Cary, R., Coulter, R., Fast, J. D., Kassianov, E. I.,
722 Kleinman, L., Laulainen, N. S., Martin, T., Paredes-Miranda, G., Pekour, M. S., Shaw, W. J.,
723 Smith, D. F., and Springston, S. R.: The T1-T2 study: evolution of aerosol properties downwind
724 of Mexico City, *Atmospheric Chem. Phys. Discuss.*, 6 (6), 12967-12999.,
725 <https://doi.org/10.5194/acp-7-1585-2007>, 2007.
- 726 Draxler, R.R., R., G. D.: HYSPLIT (HYbrid Single-Particle Lagrangian Integrated Trajectory)
727 Model, 2010.
- 728 Edgerton, S. A., Bian, X., Doran, J. C., Fast, J. D., Hubbe, J. M., Malone, E. L., Shaw, W. J.,
729 Whiteman, C. D., Zhong, S., Arriaga, J. L., Ortiz, E., Ruiz, M., Sosa, G., Vega, E., Limon, T.,
730 Guzman, F., Archuleta, J., Bossert, J. E., Elliot, S. M., Lee, J. T., McNair, L. A., Chow, J. C.,
731 Watson, J. G., Coulter, R. L., Doskey, P. V., Gaffney, J. S., Marley, N. A., Neff, W., and Petty,
732 R.: Particulate Air Pollution in Mexico City: A Collaborative Research Project, *J. Air Waste*
733 *Manag. Assoc.*, 49, 1221–1229, <https://doi.org/10.1080/10473289.1999.10463915>, 1999.
- 734 Espinosa, A., Miranda, J., and Pineda, J.C: Uncertainty evaluation in correlated quantities:
735 application to elemental analysis of atmospheric aerosols, *Rev. Mex. Física*, 56 (1), 134–140,
736 2010.
- 737 Espinosa, A. A., Reyes-Herrera, J., Miranda, J., Mercado, F., Veytia, M. A., Cuautle, M., and
738 Cruz, J. I.: Development of an X-ray fluorescence spectrometer for environmental science
739 applications, *Instrum. Sci. Technol.*, 40, 603–617,
740 <https://doi.org/10.1080/10739149.2012.693560>, 2012.
- 741 Gimeno, L., Sorí, R., Vázquez, M., Stojanovic, M., Algarra, I., Eiras-Barca, J., Gimeno-Sotelo,
742 L., and Nieto, R.: Extreme precipitation events, *WIREs Water*, 9, e1611,
743 <https://doi.org/10.1002/wat2.1611>, 2022.
- 744 Hasenkopf, C. A., Veghte, D. P., Schill, G. P., Lodoysamba, S., Freedman, M. A., and Tolbert,
745 M. A.: Ice nucleation, shape, and composition of aerosol particles in one of the most polluted
746 cities in the world: Ulaanbaatar, Mongolia, *Atmos. Environ.*, 139, 222–229,
747 <https://doi.org/10.1016/j.atmosenv.2016.05.037>, 2016.
- 748 Hernández-López, A. E., Miranda Martín Del Campo, J., Mugica-Álvarez, V., Hernández-
749 Valle, B. L., Mejía-Ponce, L. V., Pineda-Santamaría, J. C., Reynoso-Cruces, S., Mendoza-
750 Flores, J. A., and Rozanes-Valenzuela, D.: A study of PM_{2.5} elemental composition in

- 751 southwest Mexico City and development of receptor models with positive matrix factorization,
752 *Rev. Int. Contam. Ambient.*, <https://doi.org/10.20937/RICA.54066>, 2020.
- 753 Hernández-López, A. E., Santos-Medina, G. L., Morton-Bermea, O., Hernández-Álvarez, E.,
754 Villalobos-Pietrini, R., and Amador-Muñoz, O.: Chemical speciation of organic compounds
755 and elemental compositions of PM_{2.5} in Mexico City: Spatial-seasonal distribution, emission
756 sources, and formation processes, *Atmospheric Res.*, 292, 106868,
757 <https://doi.org/10.1016/j.atmosres.2023.106868>, 2023.
- 758 Heymsfield, A. J., Schmitt, C., Chen, C.-C.-J., Bansemer, A., Gettelman, A., Field, P. R., and
759 Liu, C.: Contributions of the Liquid and Ice Phases to Global Surface Precipitation:
760 Observations and Global Climate Modeling, *J. Atmospheric Sci.*, 77, 2629–2648,
761 <https://doi.org/10.1175/JAS-D-19-0352.1>, 2020.
- 762 Hoose, C. and Möhler, O.: Heterogeneous ice nucleation on atmospheric aerosols: a review of
763 results from laboratory experiments, *Atmospheric Chem. Phys.*, 12, 9817–9854,
764 <https://doi.org/10.5194/acp-12-9817-2012>, 2012.
- 765 Hoose, C., Kristjánsson, J. E., and Burrows, S. M.: How important is biological ice nucleation
766 in clouds on a global scale?, *Environ. Res. Lett.*, 5, 024009, <https://doi.org/10.1088/1748-9326/5/2/024009>, 2010.
- 768 Houze, R. A.: *Cloud dynamics*, Second edition., Academic Press, Oxford, England, 2014.
- 769 Hurtado, L., Rodríguez, G., López, J., Castillo, J. E., Molina, L., Zavala, M., and Quintana, P.
770 J. E.: Characterization of atmospheric bioaerosols at 9 sites in Tijuana, Mexico, *Atmos.
771 Environ.*, 96, 430–436, <https://doi.org/10.1016/j.atmosenv.2014.07.018>, 2014.
- 772 Población: <https://www.inegi.org.mx/temas/estructura/>, last access: 10 October 2025.
- 773 Jahl, L. G., Brubaker, T. A., Polen, M. J., Jahn, L. G., Cain, K. P., Bowers, B. B., Fahy, W. D.,
774 Graves, S., and Sullivan, R. C.: Atmospheric aging enhances the ice nucleation ability of
775 biomass-burning aerosol, *Sci. Adv.*, 7, <https://doi.org/10.1126/sciadv.abd3440>, 2021.
- 776 Jahn, L. G., Polen, M. J., Jahl, L. G., Brubaker, T. A., Somers, J., and Sullivan, R. C.: Biomass
777 combustion produces ice-active minerals in biomass-burning aerosol and bottom ash, *Proc.
778 Natl. Acad. Sci.*, 117, 21928–21937, <https://doi.org/10.1073/pnas.1922128117>, 2020.
- 779 Jáuregui, E.: *El clima de la Ciudad de México*, 1. ed., Instituto de Geografía, UNAM : Plaza y
780 Valdés Editores, México, D.F, 131 pp., 2000.
- 781 Kanji, Z. A., Ladino, L. A., Wex, H., Boose, Y., Burkert-Kohn, M., Cziczo, D. J., and Krämer,
782 M.: Overview of Ice Nucleating Particles, *Meteorol. Monogr.*, 58, 1.1-1.33,
783 <https://doi.org/10.1175/AMSMONOGRAPHIS-D-16-0006.1>, 2017.
- 784 Knopf, D. A., Wang, B., Laskin, A., Moffet, R. C., and Gilles, M. K.: Heterogeneous nucleation
785 of ice on anthropogenic organic particles collected in Mexico City, *Geophys. Res. Lett.*, 37,
786 2010GL043362, <https://doi.org/10.1029/2010GL043362>, 2010.
- 787 Knopf, D. A., Alpert, P. A., Wang, B., and Aller, J. Y.: Stimulation of ice nucleation by marine
788 diatoms, *Nat. Geosci.*, 4, 88–90, <https://doi.org/10.1038/ngeo1037>, 2011.

- 789 Kunert, A. T., Pöhlker, M. L., Tang, K., Krevert, C. S., Wieder, C., Speth, K. R., Hanson, L.
790 E., Morris, C. E., Schmale Iii, D. G., Pöschl, U., and Fröhlich-Nowoisky, J.: Macromolecular
791 fungal ice nuclei in *Fusarium*: effects of physical and chemical processing, *Biogeosciences*,
792 16, 4647–4659, <https://doi.org/10.5194/bg-16-4647-2019>, 2019.
- 793 Ladino, L. A., Raga, G. B., and Baumgardner, D.: On particle-bound polycyclic aromatic
794 hydrocarbons (PPAH) and links to gaseous emissions in Mexico City, *Atmos. Environ.*, 194,
795 31–40, <https://doi.org/10.1016/j.atmosenv.2018.09.022>, 2018.
- 796 Lezama, J. L. and Vargas, V. I.: Las fuerzas rectoras de la contaminación del aire en la Ciudad
797 de México, MIT Integr. Program Urban Reg. Glob. Air Pollut. Rep. NO8 Camb. MA, 2000.
- 798 Li, C., Zwiers, F., Zhang, X., Chen, G., Lu, J., Li, G., Norris, J., Tan, Y., Sun, Y., and Liu,
799 M.: Larger Increases in More Extreme Local Precipitation Events as Climate Warms,
800 *Geophys. Res. Lett.*, 46, 6885–6891, <https://doi.org/10.1029/2019GL082908>, 2019.
- 801 Li, M., Qi, J., Zhang, H., Huang, S., Li, L., and Gao, D.: Concentration and size distribution of
802 bioaerosols in an outdoor environment in the Qingdao coastal region, *Sci. Total Environ.*, 409,
803 3812–3819, <https://doi.org/10.1016/j.scitotenv.2011.06.001>, 2011.
- 804 Mason, R. H., Chou, C., McCluskey, C. S., Levin, E. J. T., Schiller, C. L., Hill, T. C. J.,
805 Huffman, J. A., DeMott, P. J., and Bertram, A. K.: The micro-orifice uniform deposit impactor–
806 droplet freezing technique (MOUDI-DFT) for measuring concentrations of ice nucleating
807 particles as a function of size: improvements and initial validation, *Atmospheric Meas. Tech.*,
808 8, 2449–2462, <https://doi.org/10.5194/amt-8-2449-2015>, 2015.
- 809 Mason, R. H., Si, M., Chou, C., Irish, V. E., Dickie, R., Elizondo, P., Wong, R., Brintnell, M.,
810 Elsasser, M., Lassar, W. M., Pierce, K. M., Leitch, W. R., MacDonald, A. M., Platt, A., Toom-
811 Sauntry, D., Sarda-Estève, R., Schiller, C. L., Suski, K. J., Hill, T. C. J., Abbatt, J. P. D.,
812 Huffman, J. A., DeMott, P. J., and Bertram, A. K.: Size-resolved measurements of ice-
813 nucleating particles at six locations in North America and one in Europe, *Atmospheric Chem.*
814 *Phys.*, 16, 1637–1651, <https://doi.org/10.5194/acp-16-1637-2016>, 2016.
- 815 Melchum, A., Córdoba, F., Salinas, E., Martínez, L., Campos, G., Rosas, I., Garcia-Mendoza,
816 E., Olivos-Ortiz, A., Raga, G. B., Pizano, B., Silva, Ma. M., and Ladino, L. A.: Maritime and
817 continental microorganisms collected in Mexico: An investigation of their ice-nucleating
818 abilities, *Atmospheric Res.*, 293, 106893, <https://doi.org/10.1016/j.atmosres.2023.106893>,
819 2023.
- 820 Met Office, 2023, "Microclimates," National Meteorological Library and Archive Factsheet 14,
821 [https://www.metoffice.gov.uk/binaries/content/assets/metofficegovuk/pdf/research/library-](https://www.metoffice.gov.uk/binaries/content/assets/metofficegovuk/pdf/research/library-and-archive/library/publications/factsheets/factsheet_14-microclimates_2023.pdf)
822 [and-archive/library/publications/factsheets/factsheet_14-microclimates_2023.pdf](https://www.metoffice.gov.uk/binaries/content/assets/metofficegovuk/pdf/research/library-and-archive/library/publications/factsheets/factsheet_14-microclimates_2023.pdf), last access:
823 17 February 2026.
- 824 Molina, H., Yang, Y., Ruch, T., Kim, J.-W., Mortensen, P., Otto, T., Nalli, A., Tang, Q.-Q.,
825 Lane, M. D., Chaerkady, R., and Pandey, A.: Temporal Profiling of the Adipocyte Proteome
826 during Differentiation Using a Five-Plex SILAC Based Strategy, *J. Proteome Res.*, 8, 48–58,
827 <https://doi.org/10.1021/pr800650r>, 2009.
- 828 Molina, L. T., Madronich, S., Gaffney, J. S., Apel, E., De Foy, B., Fast, J., Ferrare, R., Herndon,
829 S., Jimenez, J. L., Lamb, B., Osornio-Vargas, A. R., Russell, P., Schauer, J. J., Stevens, P. S.,
830 Volkamer, R., and Zavala, M.: An overview of the MILAGRO 2006 Campaign: Mexico City

- 831 emissions and their transport and transformation, *Atmospheric Chem. Phys.*, 10, 8697–8760,
832 <https://doi.org/10.5194/acp-10-8697-2010>, 2010.
- 833 Molina, M. J. and Molina, L. T.: Megacities and Atmospheric Pollution, *J. Air Waste Manag.*
834 *Assoc.*, 54, 644–680, <https://doi.org/10.1080/10473289.2004.10470936>, 2004.
- 835 Moreno, T., Querol, X., Pey, J., Minguillón, M. C., Pérez, N., Alastuey, A., Bernabé, R. M.,
836 Blanco, S., Cárdenas, B., Eichinger, W., Salcido, A., and Gibbons, W.: Spatial and temporal
837 variations in inhalable CuZnPb aerosols within the Mexico City pollution plume, *J. Environ.*
838 *Monit.*, 10, 370, <https://doi.org/10.1039/b716507b>, 2008.
- 839 Mülmenstädt, J., Sourdeval, O., Delanoë, J., and Quaas, J.: Frequency of occurrence of rain
840 from liquid-, mixed-, and ice-phase clouds derived from A-Train satellite retrievals, *Geophys.*
841 *Res. Lett.*, 42, 6502–6509, <https://doi.org/10.1002/2015GL064604>, 2015.
- 842 Ohneiser, K., Seifert, P., Schimmel, W., Senf, F., Gaudek, T., Radenz, M., Teisseire, A.,
843 Ettrichrätz, V., Vogl, T., Mahernndl, N., Pfeifer, N., Henneberger, J., Miller, A. J., Omanovic,
844 N., Fuchs, C., Zhang, H., Ramelli, F., Spirig, R., Kötsche, A., Kalesse-Los, H., Maahn, M.,
845 Corden, H., Berne, A., Hajipour, M., Griesche, H., Hofer, J., Engelmann, R., Skupin, A.,
846 Ansmann, A., and Baars, H.: Impact of seeder-feeder cloud interaction on precipitation
847 formation: a case study based on extensive remote-sensing, in situ and model data, *Atmospheric*
848 *Chem. Phys.*, 25, 17363–17386, <https://doi.org/10.5194/acp-25-17363-2025>, 2025.
- 849 Pereira, D. L., Silva, Ma. M., García, R., Raga, G. B., Alvarez-Ospina, H., Carabali, G., Rosas,
850 I., Martinez, L., Salinas, E., Hidalgo-Bonilla, S., and Ladino, L. A.: Characterization of ice
851 nucleating particles in rainwater, cloud water, and aerosol samples at two different tropical
852 latitudes, *Atmospheric Res.*, 250, 105356, <https://doi.org/10.1016/j.atmosres.2020.105356>,
853 2021.
- 854 Petters, M. D. and Wright, T. P.: Revisiting ice nucleation from precipitation samples: ICE
855 NUCLEATION FROM PRECIPITATION, *Geophys. Res. Lett.*, 42, 8758–8766,
856 <https://doi.org/10.1002/2015GL065733>, 2015.
- 857 Pinto, D. M., Blande, J. D., Souza, S. R., Nerg, A.-M., and Holopainen, J. K.: Plant Volatile
858 Organic Compounds (VOCs) in Ozone (O₃) Polluted Atmospheres: The Ecological Effects, *J.*
859 *Chem. Ecol.*, 36, 22–34, <https://doi.org/10.1007/s10886-009-9732-3>, 2010.
- 860 Prenni, A. J., DeMott, P. J., Sullivan, A. P., Sullivan, R. C., Kreidenweis, S. M., and Rogers,
861 D. C.: Biomass burning as a potential source for atmospheric ice nuclei: Western wildfires and
862 prescribed burns, *Geophys. Res. Lett.*, 39, <https://doi.org/10.1029/2012gl051915>, 2012.
- 863 Purdy, J. C., Austin, G. L., Seed, A. W., and Cluckie, I. D.: Radar evidence of orographic
864 enhancement due to the seeder feeder mechanism, *Meteorol. Appl.*, 12, 199–206,
865 <https://doi.org/10.1017/S1350482705001672>, 2005.
- 866 Querol, X., Pey, J., Minguillón, M. C., Pérez, N., Alastuey, A., Viana, M., Moreno, T., Bernabé,
867 R. M., Blanco, S., Cárdenas, B., Vega, E., Sosa, G., Escalona, S., Ruiz, H., and Artíñano, B.:
868 PM speciation and sources in Mexico during the MILAGRO-2006 Campaign, *Atmospheric*
869 *Chem. Phys.*, 8, 111–128, <https://doi.org/10.5194/acp-8-111-2008>, 2008.
- 870 Querol, X., Tobías, A., Pérez, N., Karanasiou, A., Amato, F., Stafoggia, M., Pérez García-
871 Pando, C., Ginoux, P., Forastiere, F., Gumy, S., Mudu, P., and Alastuey, A.: Monitoring the

- 872 impact of desert dust outbreaks for air quality for health studies, *Environ. Int.*, 130, 104867,
873 <https://doi.org/10.1016/j.envint.2019.05.061>, 2019.
- 874 Raga, G. B., Ladino, L. A., Baumgardner, D., Ramirez-Romero, C., Córdoba, F., Alvarez-
875 Ospina, H., Rosas, D., Amador, T., Miranda, J., Rosas, I., Jaramillo, A., Yakobi-Hancock, J.,
876 Kim, J. S., Martínez, L., Salinas, E., and Figueroa, B.: ADABBOY: African Dust And Biomass
877 Burning Over Yucatan, *Bull. Am. Meteorol. Soc.*, 102, E1543–E1556,
878 <https://doi.org/10.1175/BAMS-D-20-0172.1>, 2021.
- 879 Reynoso-Cruces, S., Miranda-Martín-Del-Campo, J., and Pineda-Santamaría, J. C.: Elemental
880 composition of PM₁₀ in indoor environments of a scientific research institution and risk
881 assessment, *Environ. Pollut. Bioavailab.*, 35, 2232108,
882 <https://doi.org/10.1080/26395940.2023.2232108>, 2023.
- 883 Riojas-Rodríguez, H., Álamo-Hernández, U., Texcalac-Sangrador, J. L., and Romieu, I.: Health
884 impact assessment of decreases in PM₁₀ and ozone concentrations in the Mexico City
885 Metropolitan Area. A basis for a new air quality management program, *Salud Pública México*,
886 56, 579, <https://doi.org/10.21149/spm.v56i6.7384>, 2014.
- 887 Ríos, B. and Raga, G. B.: Spatio-temporal distribution of burned areas by ecoregions in Mexico
888 and Central America, *Int. J. Remote Sens.*, 39, 949–970,
889 <https://doi.org/10.1080/01431161.2017.1392641>, 2018.
- 890 Rodríguez-Gómez, C.: Variabilidad de los núcleos de glaciación en la capa límite y la tropósfera
891 libre en Altzomoni, y su influencia en la formación de nubes mixtas, Universidad Nacional
892 Autónoma de México, México, CDMX, 128 pp., 2021.
- 893 Rodriguez-Gomez, C., Ramirez-Romero, C., Cordoba, F., Raga, G. B., Salinas, E., Martinez,
894 L., Rosas, I., Quintana, E. T., Maldonado, L. A., Rosas, D., Amador, T., Alvarez, H., and
895 Ladino, L. A.: Characterization of culturable airborne microorganisms in the Yucatan
896 Peninsula, *Atmos. Environ.*, 223, 117183, <https://doi.org/10.1016/j.atmosenv.2019.117183>,
897 2020.
- 898 Rogers, R. R. and Yau, M. K.: A short course in cloud physics, Third edition., Butterworth-
899 Heinemann, Burlington, Massachusetts, 1 pp., 1996.
- 900 Rosas, D., Silva, M. M., Figueroa, B., Morton-Bermea, O., Miranda, J., Alvarez, H., Puig, T.
901 P., Morales, J., Uuh, J., Hernández-Alvarez, E., Novelo, S., Olivares, J., Salcedo, D., Rosas, I.,
902 Ponce, C., Raga, G. B., and Ladino, L. A.: African dust particles over the western Caribbean:
903 Chemical characterization, *Atmos. Environ.*, 347, 121095,
904 <https://doi.org/10.1016/j.atmosenv.2025.121095>, 2025.
- 905 Russy-Velandia, L., Ramírez, O., Barrera, J., Mendoza-Téllez, S., Álvarez, H., Patiño, M. C.,
906 and Ladino, L. A.: Approach to culturable bioaerosols and their environmental drivers at a
907 border site in the northwestern Amazon, *Atmospheric Environ. X*, 27, 100362,
908 <https://doi.org/10.1016/j.aeaoa.2025.100362>, 2025.
- 909 Salcido, A., Carreón-Sierra, S., Georgiadis, T., Celada-Murillo, A.-T., and Castro, T.: Lattice
910 Wind Description and Characterization of Mexico City Local Wind Events in the 2001–2006
911 Period, *Climate*, 3, 542–562, <https://doi.org/10.3390/cli3030542>, 2015.

- 912 Schnell, R. C. and Vali, G.: Biogenic Ice Nuclei: Part I. Terrestrial and Marine Sources, *J.*
913 *Atmospheric Sci.*, 33, 1554–1564, <https://doi.org/10.1175/1520->
914 [0469\(1976\)033%253C1554:BINPIT%253E2.0.CO;2](https://doi.org/10.1175/1520-0469(1976)033%253C1554:BINPIT%253E2.0.CO;2), 1976.
- 915 Shardt, N., Isenrich, F. N., Waser, B., Marcolli, C., Kanji, Z. A., deMello, A. J., and Lohmann,
916 U.: Homogeneous freezing of water droplets for different volumes and cooling rates, *Phys.*
917 *Chem. Chem. Phys.*, 24, 28213–28221, <https://doi.org/10.1039/D2CP03896J>, 2022.
- 918 Tabari, H.: Climate change impact on flood and extreme precipitation increases with water
919 availability, *Sci. Rep.*, 10, 13768, <https://doi.org/10.1038/s41598-020-70816-2>, 2020.
- 920 Tarn, M. D., Sikora, S. N. F., Porter, G. C. E., Shim, J., and Murray, B. J.: Homogeneous
921 Freezing of Water Using Microfluidics, *Micromachines*, 12, 223,
922 <https://doi.org/10.3390/mi12020223>, 2021.
- 923 Toll, V., Rahu, J., Keernik, H., Trofimov, H., Voormansik, T., Manshausen, P., Hung, E.,
924 Michelson, D., Christensen, M. W., Post, P., Junninen, H., Murray, B. J., Lohmann, U., Watson-
925 Parris, D., Stier, P., Donaldson, N., Storelvmo, T., Kulmala, M., and Bellouin, N.: Glaciation
926 of liquid clouds, snowfall, and reduced cloud cover at industrial aerosol hot spots, *Science*, 386,
927 756–762, <https://doi.org/10.1126/science.adl0303>, 2024.
- 928 Trofimov, H., Post, P., Gryspeerdt, E., and Toll, V.: Meteorological Conditions Favorable for
929 Strong Anthropogenic Aerosol Impacts on Clouds, *J. Geophys. Res. Atmospheres*, 127,
930 e2021JD035871, <https://doi.org/10.1029/2021JD035871>, 2022.
- 931 Vali, G.: Ice Nucleation — a review, in: *Nucleation and Atmospheric Aerosols 1996*, Elsevier,
932 271–279, <https://doi.org/10.1016/B978-008042030-1/50066-4>, 1996.
- 933 Vega, E., Reyes, E., Ruiz, H., García, J., Sánchez, G., Martínez-Villa, G., González, U., Chow,
934 J. C., and Watson, J. G.: Analysis of PM_{2.5} and PM₁₀ in the Atmosphere of Mexico City during
935 2000–2002, *J. Air Waste Manag. Assoc.*, 54, 786–798,
936 <https://doi.org/10.1080/10473289.2004.10470952>, 2004.
- 937 Wex, H., Augustin-Bauditz, S., Boose, Y., Budke, C., Curtius, J., Diehl, K., Dreyer, A., Frank,
938 F., Hartmann, S., Hiranuma, N., Jantsch, E., Kanji, Z. A., Kiselev, A., Koop, T., Möhler, O.,
939 Niedermeier, D., Nillius, B., Rösch, M., Rose, D., Schmidt, C., Steinke, I., and Stratmann, F.:
940 Intercomparing different devices for the investigation of ice nucleating particles using Snomax[®]
941 as test substance, *Atmospheric Chem. Phys.*, 15, 1463–1485, <https://doi.org/10.5194/acp-15->
942 [1463-2015](https://doi.org/10.5194/acp-15-1463-2015), 2015.
- 943 Zhao, B., Wang, Y., Gu, Y., Liou, K.-N., Jiang, J. H., Fan, J., Liu, X., Huang, L., and Yung, Y.
944 L.: Ice nucleation by aerosols from anthropogenic pollution, *Nat. Geosci.*, 12, 602–607,
945 <https://doi.org/10.1038/s41561-019-0389-4>, 2019.
- 946 Zhu, Z., Peng, C., Li, X., Zhang, R., Dai, X., Jiang, B., and Chen, J.: Remote Sensing-Based
947 Analysis of Precipitation Events: Spatiotemporal Characterization across China, *Water*, 16,
948 2345, <https://doi.org/10.3390/w16162345>, 2024.
- 949